Supplementary material

1. Material decomposition

Beer-Lambert equation

$$I(x,y,z_o,E) = I_o(x,y,0,E)e^{-\int_0^{z_o} \mu(x,y,z,E)dz},$$

(S1)

where $I(x,y,z_o,E)$ and $I_o(x,y,0,E)$ are intensities after and before traverse the sample, z_o is the thickness of the sample, E is the energy of the X-ray beam, and μ is the attenuation coefficient. For a breast tissue with micro-calcifications, the integral term can be written as:

$$\int_0^{z_o} \mu(x,y,z,E)dz = \mu_1(E)\int_0^{z_o} g_1(x,y,z)dz + \mu_2(E)\int_0^{z_o} g_2(x,y,z)dz + \mu_B(E)\int_0^{z_o} g_B(x,y,z)dz,$$

(S2)

with $\mu_1(E)$, $\mu_2(E)$ as the attenuation coefficients of two types of micro-calcifications, and $\mu_B(E)$ as the attenuation coefficient of the breast tissue. The energy-independent integrals, $\int_0^{z_o} g_i(x,y,z)dz$, correspond to the projected thickness of each material. If $\int_0^{z_o} g_T(x,y,z)dz = \int_0^{z_o} g_1(x,y,z)dz + \int_0^{z_o} g_2(x,y,z)dz + \int_0^{z_o} g_B(x,y,z)dz$ is the total projected thickness of the sample, then the Beer-Lambert equation is

$$I(x,y,z_o,E) = I_o(x,y,0,E)e^{-\mu_B(E)\int_0^{z_o} g_T(x,y,z)dz - \Delta\mu_1(E)\int_0^{z_o} g_1(x,y,z)dz - \Delta\mu_2(E)\int_0^{z_o} g_2(x,y,z)dz},$$

(S3)

$$f(E) = -\ln\left(\frac{I_o(x,y,0,E)}{I(x,y,z_o,E)e^{-\mu_B(E)\int_0^{z_o} g_T(x,y,z)dz}}\right) = \Delta\mu_1(E)\int_0^{z_o} g_1(x,y,z)dz + \Delta\mu_2(E)\int_0^{z_o} g_2(x,y,z)dz,$$

(S4)

n images at different energies, $f(E_i)$, are taken to retrieve $\int_0^{z_o} g_1(x,y,z)dz$ and $\int_0^{z_o} g_2(x,y,z)dz$ using matricial methods as:

$$f(E_1) = \Delta\mu_1(E_1)\int_0^{z_o} g_1(x,y,z)dz + \Delta\mu_2(E_1)\int_0^{z_o} g_2(x,y,z)dz$$

$$f(E_2) = \Delta\mu_1(E_2)\int_0^{z_o} g_1(x,y,z)dz + \Delta\mu_2(E_2)\int_0^{z_o} g_2(x,y,z)dz$$

$$\vdots$$

$$f(E_n) = \Delta\mu_1(E_n)\int_0^{z_o} g_1(x,y,z)dz + \Delta\mu_2(E_n)\int_0^{z_o} g_2(x,y,z)dz$$

$$\begin{pmatrix} \Delta\mu_1(E_1) & \Delta\mu_2(E_1) \\ \vdots & \vdots \\ \Delta\mu_1(E_n) & \Delta\mu_2(E_n) \end{pmatrix} \begin{pmatrix} \int_0^{z_o} g_1(x,y,z)dz \\ \int_0^{z_o} g_2(x,y,z)dz \end{pmatrix} = \begin{pmatrix} f(E_1) \\ \vdots \\ f(E_n) \end{pmatrix} \rightarrow \mathrm{B H} = \Gamma \qquad (S5)$$

And inverting the matrix equation for H as

$$\mathrm{B}^T \mathrm{B H} = \mathrm{B}^T \Gamma$$

$$(\mathrm{B}^T \mathrm{B})^{-1} \mathrm{B}^T \mathrm{B H} = (\mathrm{B}^T \mathrm{B})^{-1} \mathrm{B}^T \Gamma \rightarrow \mathrm{H} = (\mathrm{B}^T \mathrm{B})^{-1} \mathrm{B}^T \Gamma \qquad (S6)$$

Verification of equation S6

Images were acquired for two types of micro-calcifications—alumina and hydroxyapatite (HA)—at five different radii, embedded in a standard breast tissue with a thickness of 5 cm. The corresponding imaging energies were 20 keV, 24 keV and 28 keV (Figure S_1), forming a 3×1 matrix for Γ. The objective is to retrieve the projected thickness of alumina and HA, using their attenuation coefficients at these energies to construct the matrix B.
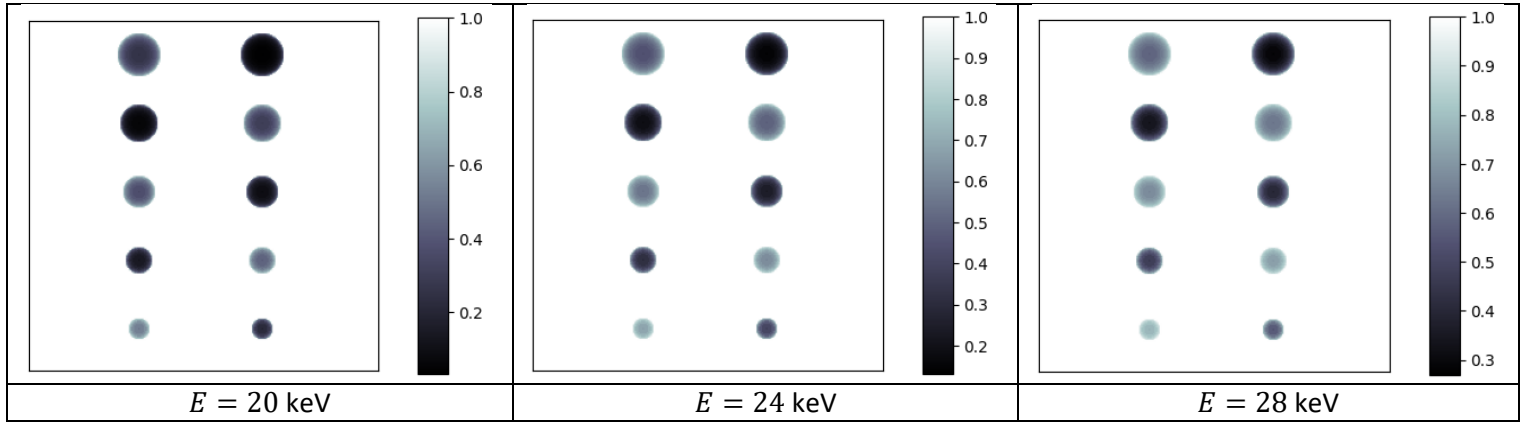

Figure S_1. Images acquired at 20 keV, 24 keV and 28 keV of standard breast tissue with micro-calcifications of alumina and hydroxyapatite of five different radii.1
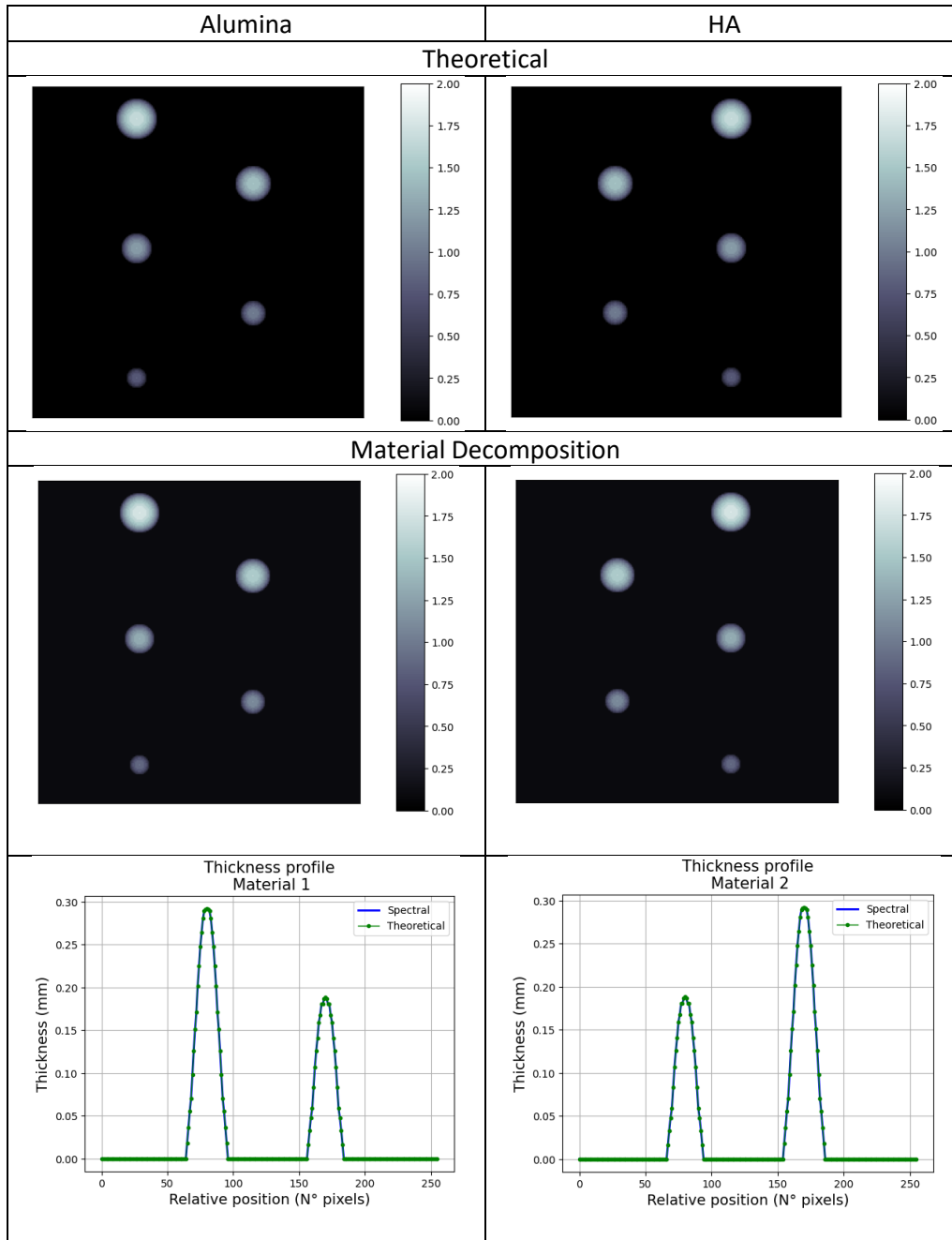
Figure S_2. Projected thickness maps of Alumina and HA, retrieved by using equation S6 (Second row). A comparison with the theoretical projected thickness maps (First row) is given with the profiles thickness profiles (Third row).

The results are presented in Figure S_2, where the algorithm successfully retrieves the projected thickness of both materials. A comparison between the expected and retrieved projected thickness profiles—obtained by projecting the projected thickness images along the horizontal axis—is shown for both materials.

2. Simulation-Materials

Material	Density $(\frac{g}{cm^3})$	Chemical formula
Hydroxyapatite	3.160	$Ca_{10}(PO_4)_6(OH)_2$
Alumina	3.950	Al_2O_3
Silicone	0.970	C_2H_6OSi
PMMA	1.195	$C_5O_2H_8$
Wax (Eicosane)	0.788	$C_{20}H_{42}$

Table S_1. Information of materials used in GATE, providing their density and their chemical formula [R1].

Material	Density $(\frac{g}{cm^3})$	Elemental weight
Fibro Glandular	1.020	H=10.6%, C=33.2%, N=3.0%, O=52.7%, Na=0.1%, S=0.2%, Cl=0.1%, P=0.1%
Adipose	0.950	H=11.4%, C=59.8%, N=0.7%, O=27.8%, Na=0.1%, S=0.1%, Cl=0.1%

Table S_2. Information of the material Fibroglandular and Adipose used in GATE, providing their density and their elemental weight according to [R2].

3. Characterization of the Timepix3 detector
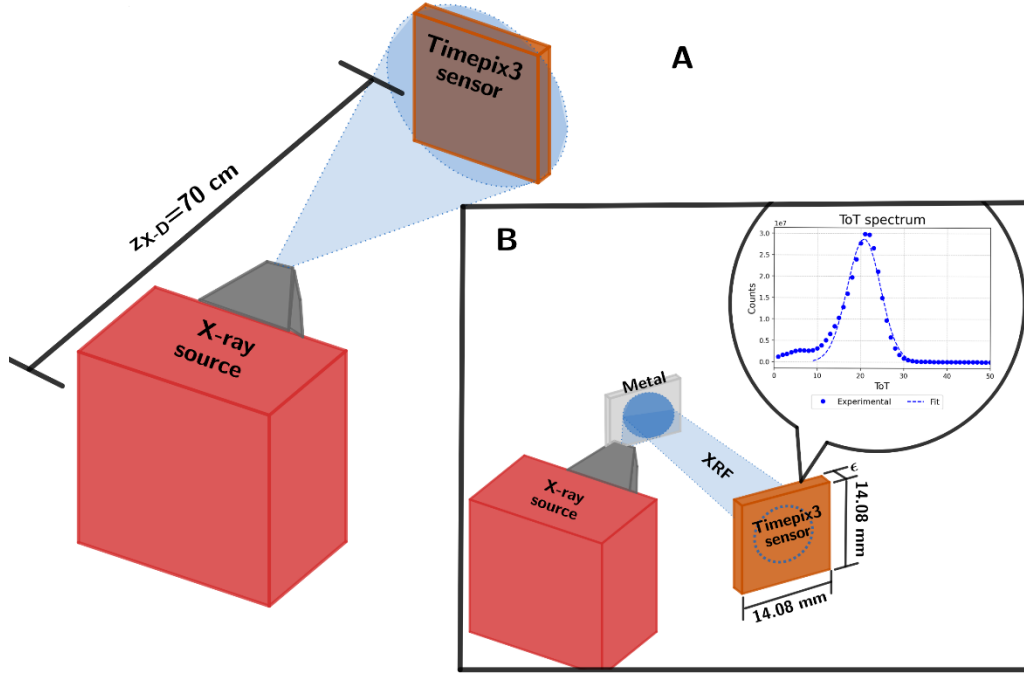### 1) ToT vs. E. Using Timepix3 in Pixel mode.

Figure S_3. Panel A: General diagram of dose measurement, illustrating the X-ray source and detector. Panel B: General diagram used for characterization of the Timepix3 detector, to convert ToT to energy values. The detector is arranged so that a metal can read the fluorescence photons generated by it. The ToT distribution obtained for comparison.

The Timepix3 is a photon-counting detector that combines a 130 nm CMOS readout chip with a 1 mm thick CdTe crystal serving as the X-ray sensor [R3]. The sensor consists of a 256×256 matrix of square pixels with a pixel pitch of 55 um, resulting in a total detection area of about 14.08 mm × 14.08 mm. The detector operates in two measurement modes: the counting mode and the ToT (Time-over-Threshold)-ToA (Time of Arrival) mode. In the ToT-ToA mode, the ToA value is obtained by counting the total periods before the signal crosses the threshold, and the ToT value is determined by counting the periods while the signal remains above the threshold [R3]. Initially, charge sharing in the detector, where the generated charge by a photon in a pixel is spread among its adjacent pixels, is the reason for incorrectly reconstructing the ToT values at each pixel. This problem is solved by using a clustering algorithm [R4], which relates pixel clusters close in space and time to reconstruct the correct ToT value in each pixel.

The ToT value is proportional to the energy of the incident photon [R3,R5]. The relationship between ToT and energy is calibrated as follows [R5]: first, a ToT spectrum for a reference metal is acquired in ToT-ToA mode, with the detector arranged as illustrated in Panel B – Figure S_3. The ToT value corresponding to the peak count is identified and associated with the X-ray fluorescence energy of that metal. Using four metals, such as Zr (15.775 keV), Rh (20.216 keV), Sn (25.271 keV), and Gd (42.996 keV), determining their respective ToT peak values (Left of Figure S_4), a calibration curve relating ToT peaks to photon energy is established (Right of Figure S_4).
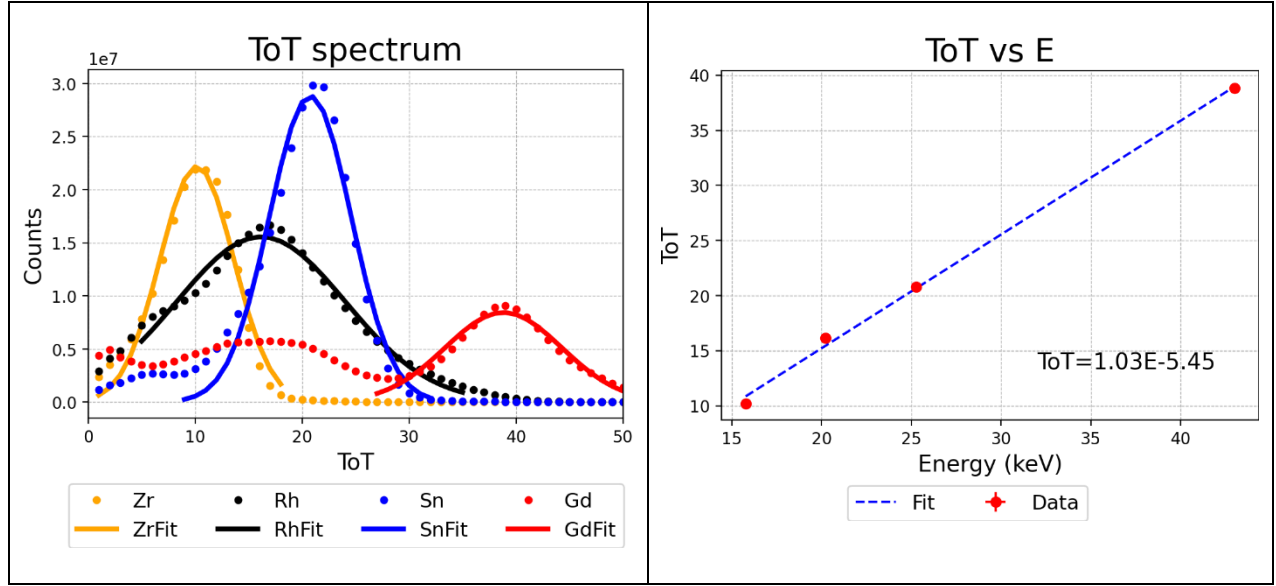
Figure S_4. Left. ToT spectrum of four materials. Right. Calibration curve of ToT with energy.

2) Spectrum of the X-ray source using the Timepix3.

One of the advantages of measuring the energy of the incident photons is the possibility to estimate entrance radiation doses at any distance between the X-ray source and the detector. The incident spectrum on the detector $S(E')$ is measured when the Timepix3 is placed at 70 cm from the X-ray source (Panel A – Figure S_3). Following the process described in [R6], $S(E')$ could be obtained in the following way:

$$M_E = \sum_{E'} U_{EE'} S_{E'}$$ (S7)

- M_E: Energy spectrum measured by the detector
- $S_{E'}$: Spectrum of the X-ray source
- $U_{EE'}$: Detector response function

$U_{EE'}$ is determined by using the energy resolution of the detector. This resolution is determined by the fluorescence spectra of four materials: Zr ($E_{\alpha_1} = 15.775$ keV), Sn ($E_{\alpha_1} = 25.271$ keV), Gd ($E_{\alpha_1} = 42.996$ keV), Am_{241} ($E_{\gamma} = 59.541$ keV), as follows:

- Perform a Gaussian fit around the peaks of the spectrum (Left of Figure S_5)
- Obtain σ and E_o from each fit to obtain the energy resolution from each material.
  $$\rightarrow R_E = \frac{FWHM}{E_o} = \frac{2\sqrt{2\ln 2}\,\sigma}{E_o}$$
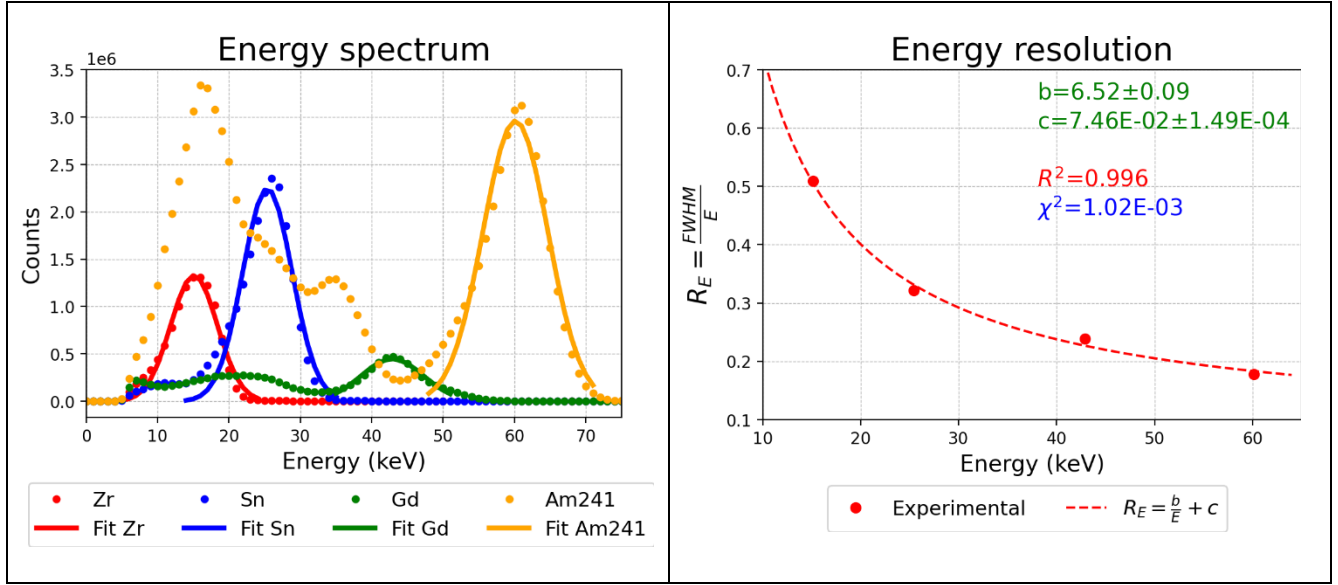- Graph of R_E vs E (Right of Figure S_5)

Figure S_5. Left. Energy spectrum of four materials, with Gaussian fits. Right. Dependence of Energy resolution of the detector with energy

Each element of $U_{EE'}$ is constructed from Gaussian functions, following the energy dependence of $R_E(E)$, as illustrated in Figure 6.
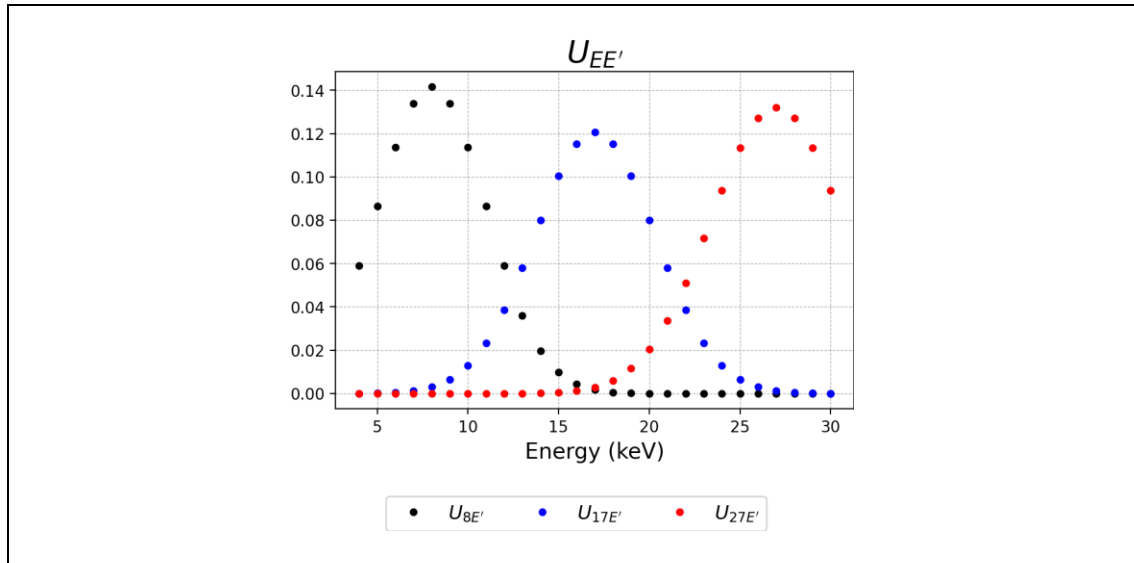

Figure S_6. Left. $U_{EE'}$ for E=8 keV (Black), E=17 keV (Blue) and E=27 keV (Red).

Measuring M_E for each spectrum, with the setup pf Panel A – Figure S_3, the Bayesian deconvolution method [R7] is used to determine S_E from equation S7, as illustrated in Figure S_7 for Rh and Al at 28 kVp.
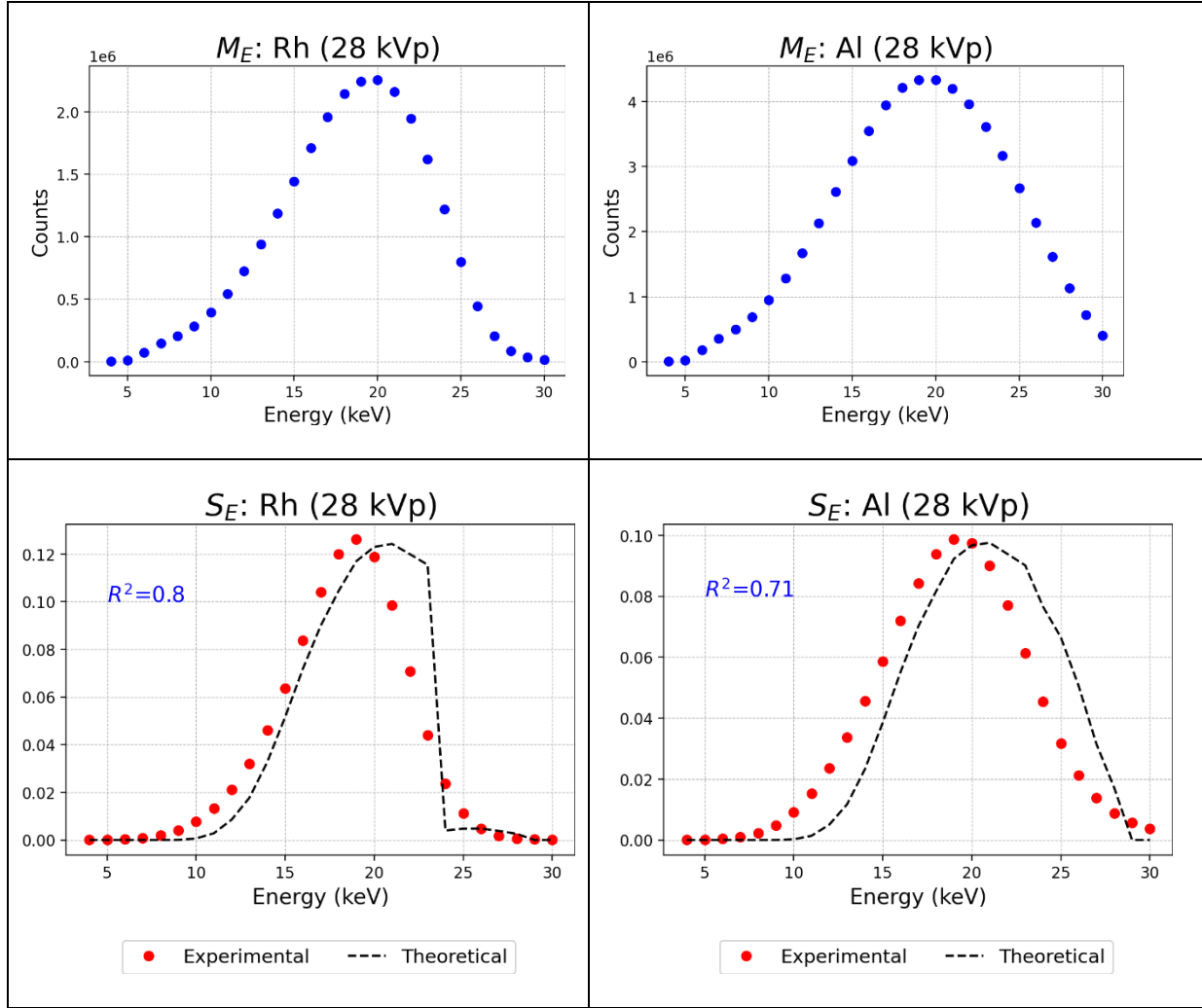
Figure S_7. Top. M_E measured for Rh and Al at 28 kVp. Bottom, S_E retrieved for Rh and Al at 28 kVp.

4. CNR error propagation

CNR is defined as:

$$CNR = \frac{|\bar{I}_S - \bar{I}_B|}{\sigma_B} \tag{S8}$$

where $\bar{I}_S$ represents the average intensity in the region of the μC, while $\bar{I}_B$ and σ_B represent the average intensity and the standard deviation in the region with no μC, respectively. Rewriting each term of equation S8, then:

$$CNR = \frac{\left| \frac{1}{N_{PS}} \sum_{i=1}^{N_{PS}} I_{iS} - \frac{1}{N_{PB}} \sum_{i=1}^{N_{PB}} I_{iB} \right|}{\sqrt{\frac{1}{N_{PB}} \sum_{i=1}^{N_{PB}} I_{iB}^2 - \frac{1}{N_{PB}^2} \left(\sum_{i=1}^{N_{PB}} I_{iB} \right)^2}} \tag{S9}$$

where I_{iS} and N_{PS} (I_{iB} and N_{PB}) represent the intensity in the i-th pixel and the number of pixels in the region with (without) μC, respectively. The intensities I_{iS} and I_{iB} can be expressed in terms of number of counts in the RAW image (R_i) and the FF image (F_i) as $I_{iS} = \frac{R_{iS}}{F_{iS}}$ and $I_{iB} = \frac{R_{iB}}{F_{iB}}$, respectively. The variance formula is used to calculate the uncertainty in CNR as:

$$\sigma_{CNR} = \sqrt{\sum_{i=1}^{N_{PS}} \left(\frac{\partial CNR}{\partial I_{iS}} \right)^2 \sigma_{I_{iS}}^2 + \sum_{i=1}^{N_{PB}} \left(\frac{\partial CNR}{\partial I_{iB}} \right)^2 \sigma_{I_{iB}}^2} \tag{S10}$$

where the uncertainties in the intensities for the i-th pixel, $\sigma_{I_{iS}}$ and $\sigma_{I_{iB}}$, using the variance formula as:

$$\sigma_{I_{iS}} = \sqrt{\left(\frac{\partial I_{iS}}{\partial R_{iS}} \right)^2 \sigma_{R_{iS}}^2 + \left(\frac{\partial I_{iS}}{\partial F_{iS}} \right)^2 \sigma_{F_{iS}}^2} = I_{iS} \sqrt{\left(\frac{\sigma_{R_{iS}}}{R_{iS}} \right)^2 + \left(\frac{\sigma_{F_{iS}}}{F_{iS}} \right)^2} = I_{iS} \sqrt{\frac{1}{R_{iS}} + \frac{1}{F_{iS}}} \tag{S11}$$

$$\sigma_{I_{iB}} = \sqrt{\left(\frac{\partial I_{iB}}{\partial R_{iB}} \right)^2 \sigma_{R_{iB}}^2 + \left(\frac{\partial I_{iB}}{\partial F_{iB}} \right)^2 \sigma_{F_{iB}}^2} = I_{iB} \sqrt{\left(\frac{\sigma_{R_{iB}}}{R_{iB}} \right)^2 + \left(\frac{\sigma_{F_{iB}}}{F_{iB}} \right)^2} = I_{iB} \sqrt{\frac{1}{R_{iB}} + \frac{1}{F_{iB}}} \tag{S12}$$

The standard deviation of the number of counts is estimated using Poisson statistics. To conclude the calculation in equation S10, the derivatives are estimated from equation S9 as:

$$\frac{\partial CNR}{\partial I_{iS}} = \frac{1}{N_{PS} \sigma_B} \tag{S13}$$

$$\frac{\partial CNR}{\partial I_{iB}} = \frac{1}{N_{PB} \sigma_B} \left[1 + CNR \cdot \left(\frac{I_{iB} - \bar{I}_B}{\sigma_B} \right) \right] \tag{S14}$$

References

[R1] U. D. of commerce, "Nist. national institute of standards and technology," 2021. [Online]. Available: https://www.nist.gov/

[R2] A. Oliveira, B. A. Meguerian, and C. T. Mesquita, "Influence of breast characteristics in myocardial scintigraphy through the monte carlo method," Arquivos Brasileiros de Cardiologia, vol. 96, no. 1, 2011. [Online]. Available: https://doi.org/10.1590/s0066-782x2010005000162

[R3] T. Poikela, J. Plosila, T. Westerlund, M. Campbell, M. D. Gaspari, X. Llopart, V. Gromov, R. Kluit, M. van Beuzekom, F. Zappon, V. Zivkovic, C. Brezina, K. Desch, Y. Fu, and A. Kruth, "Timepix3: a 65k channel hybrid pixel readout chip with simultaneous toa/tot and sparse readout," Journal of Instrumentation, vol. 9, no. 05, p. C05013, may 2014. [Online]. Available: https://dx.doi.org/10.1088/1748-0221/9/05/C05013

[R4] C. Navarrete, S. Procz, M. K. Schütz, G. Roque, J. Fey, C. Avila, A. Olivo, and M. Fiederle, "Spectral x-ray phase contrast imaging with a cdte photon-counting detector," Nuclear Instruments and Methods in Physics Research, Section A: Accelerators, Spectrometers, Detectors and Associated Equipment, vol. 971, pp. 164 098–7, 8 2020. [Online]. Available: https://doi.org/10.1016/j.nima.2020.164098

[R5] J. Jakubek, "Precise energy calibration of pixel detector working in time-over-threshold mode," Nuclear Instruments and Methods in Physics Research Section A: Accelerators, Spectrometers, Detectors and Associated Equipment, vol. 633, pp. S262–S266, 2011, 11th International Workshop on Radiation Imaging Detectors (IWORID). [Online]. Available: https://doi.org/10.1016/j.nima.2010.06.183

[R6] J. U. Parra, M. Schütz, G. Roque, J. Fey, C. Avila, M. Fiederle, and S. Procz, "Dose estimation in x-ray backscatter imaging with timepix3 and tld detectors," Journal of Instrumentation, vol. 18, no. 05, p. P05042, 05 2023. [Online]. Available: https://dx.doi.org/10.1088/1748-0221/18/05/P05042

[R7] P. Sievers, T. Weber, T. Michel, J. Klammer, L. Büermann, and G. Anton, "Bayesian deconvolution as a method for the spectroscopy of x-rays with highly pixelated photon counting detectors," Journal of Instrumentation, vol. 7, no. 03, p. P03003, 03 2012. [Online]. Available: https://dx.doi.org/10.1088/1748-0221/7/03/P03003